Atmos. Meas. Tech. Discuss., 7, 12173–12217, 2014
www.atmos-meas-tech-discuss.net/7/12173/2014/
doi:10.5194/amtd-7-12173-2014

Atmospheric Measurement Techniques Discussions

A linear method for the retrieval of sun-induced chlorophyll fluorescence from GOME-2 and SCIAMACHY data

P. Köhler[1,2], **L. Guanter**[1,2], **and J. Joiner**[3]

[1]Institute for Space Sciences, Freie Universität Berlin, Berlin, Germany
[2]German Research Center for Geosciences (GFZ), Remote Sensing Section, Potsdam, Germany
[3]NASA Goddard Space Flight Center, Greenbelt, MD, USA

Received: 12 September 2014 – Accepted: 12 November 2014 – Published: 4 December 2014

Correspondence to: P. Köhler (philipp.koehler@wew.fu-berlin.de)

Published by Copernicus Publications on behalf of the European Geosciences Union.

Abstract

Global retrievals of near-infrared sun-induced chlorophyll fluorescence (SIF) have been achieved in the last years by means of a number of space-borne atmospheric spectrometers. Here, we present a new retrieval method for medium spectral resolution instruments such as the Global Ozone Monitoring Experiment (GOME-2) and the SCanning Imaging Absorption SpectroMeter for Atmospheric ChartographY (SCIAMACHY). Building upon the previous work by Joiner et al. (2013), our approach solves existing issues in the retrieval such as the non-linearity of the forward model and the arbitrary selection of the number of free parameters. In particular, we use a backward elimination algorithm to optimize the number of coefficients to fit, which reduces also the retrieval noise and selects the number of state vector elements automatically. A sensitivity analysis with simulated spectra has been utilized to evaluate the performance of our retrieval approach. The method has also been applied to estimate SIF from real spectra from GOME-2 and for the first time, from SCIAMACHY. We find a good correspondence of the absolute SIF values and the spatial patterns from the two sensors, which suggests the robustness of the proposed retrieval method. In addition, we examine uncertainties and use our GOME-2 retrievals to show empirically the low sensitivity of the SIF retrieval to cloud contamination.

1 Introduction

During the process of photosynthesis, the chlorophyll-*a* of photosynthetically-active vegetation emits a small fraction of its excess energy as an electromagnetic signal (e.g., Zarco-Tejada et al., 2003). This signal, called sun-induced chlorophyll fluorescence (SIF), takes place in the 650–800 nm spectral region. Several studies have addressed the estimation of SIF from ground-based, airborne and spaceborne spectrometers in the last decade (see Meroni et al., 2009, and references therein). Here, we focus on SIF retrieval methods from space and their achievements as

AMTD
7, 12173–12217, 2014

this work is intended to contribute to the development of this specific field. The first global SIF observations have been achieved in the last three years by studies from Joiner et al. (2011), Frankenberg et al. (2011b) and Guanter et al. (2012) using data from the Fourier Transform Spectrometer (FTS) on-board the Japanese Greenhouse Gases Observing Satellite (GOSAT). The high spectral resolution of the GOSAT-FTS (approx. 0.025 nm) enabled the possibility to evaluate the in-filling of solar Fraunhofer lines by SIF from space. Joiner et al. (2011) based their retrieval on the strong K line around 770.1 nm, while Frankenberg et al. (2011b) and Guanter et al. (2012) used both the 757 and the 770 nm spectral regions. The 757 nm spectral region contains several solar Fraunhofer lines and is devoid of significant atmospheric absorption, which minimizes the impact of atmospheric effects on the retrieval. Using only the single line in 770 nm simplifies the forward model, but it may result in noisier retrievals since the number of measurements and the intensity of fluorescence is lower with respect to the spectral region in 757 nm. The method proposed by Frankenberg et al. (2011b) relies on the physical modeling of the in-filling of solar Fraunhofer lines by SIF using the instrumental line shape function and a reference solar irradiance data set. The surface reflectance, atmospheric scattering as well as wavelength shifts have to be estimated for each measurement. Instead of explicitly modeling these parameters for each measurement, Guanter et al. (2012) proposed a data-driven approach which is based on a singular value decomposition (SVD) technique. The basic assumption for this retrieval method is that any radiance spectrum in a narrow spectral window can be expressed as a linear combination of singular vectors plus fluorescence. This technique has the advantage that it provides simpler and faster retrievals based on a linear forward model. A caveat of the statistically based approach is an arbitrary selection of the optimum number of singular vectors, which has an effect on the retrieval accuracy and precision.

One intrinsic limitation of the GOSAT-FTS data arises from the coarse resolution of global maps ($2^{\circ} \times 2^{\circ}$) which is caused by a poor spatial sampling and a relatively high retrieval noise. Therefore, it was crucial that results from Joiner et al. (2012) indicated

AMTD
7, 12173–12217, 2014

that instruments with lower spectral resolutions are also capable to estimate SIF from space. Joiner et al. (2012) examined the in-filling of the deep calcium (Ca) II solar Fraunhofer line at 866 nm by SIF using the SCanning Imaging Absorption SpectroMeter for Atmospheric CHartographY (SCIAMACHY) satellite instruments which has a spectral resolution of approximately 0.5 nm. Spatial and temporal variations of retrieved SIF were found to be consistent, although there is only a weak intensity of SIF in the examined spectral range. In this context it should be considered that the continuous spatial sampling of instruments as SCIAMACHY might be more suitable to create global maps than GOSAT, which has a lack of global coverage. For this reason, it can be presumed that the representativeness of spatially mapped SIF is enhanced by using the data from instruments which provide a continuous spatial sampling.

A further achievement has been the data-driven study of Joiner et al. (2013). They proposed another SIF retrieval method for the Global Ozone Monitoring Experiment (GOME-2). The continuous spatial sampling as well as the spectral and radiometric performance of GOME-2 measurements enables a significant increase of the spatio-temporal resolution with respect to previous works. In principle, this recently proposed approach extends the SVD (or principal component analysis, PCA) technique applied exclusively on solar Fraunhofer lines (Guanter et al., 2012) to a broader wavelength range making also use of atmospheric absorption bands (water vapor, O_2 A).

In view of the above, it can be stated that all current methods to retrieve SIF from space are united by the fact that the in-filling of solar Fraunhofer lines and/or atmospheric absorption features by SIF is evaluated.

Here, we present a new SIF retrieval method using a comparable methodology to that developed for ground-based instrumentations by Guanter et al. (2013) and for space-based measurements by Joiner et al. (2013). A feature of the method consists in the automated determination of used singular vectors and of the number of principal components (PCs), respectively. We test the proposed retrieval method to demonstrate the applicability of the retrieval method. Besides a time series of GOME-2 SIF results covering the 2007–2011 time period, we are able to present global composites of SIF

AMTD
7, 12173–12217, 2014

evaluated at 740 nm from SCIAMACHY data for the first time. We compare SIF retrieval results from GOME-2 and SCIAMACHY data as well as results obtained from GOME-2 data by Joiner et al. (2013). Furthermore, we examine uncertainties caused by noise and assess the effect of clouds on the retrieval through the analysis of different cloud filter thresholds.

2 Instruments

2.1 GOME-2

The Global Ozone Monitoring Experiment (Munro et al., 2006) is a nadir-scanning medium-resolution UV/VIS spectrometer on-board EUMETSAT's polar orbiting Meteorological Operational Satellites (MetOp-A and MetOp-B). MetOp-A (launched in October 2006) and MetOp-B (launched in September 2012) carry 13 instruments performing operational measurements of atmosphere, land and sea surface. One revolution on the sun-synchronous orbit at an altitude of approximately 820 km with an overpass time around 09:30 local solar time takes about 100 min. GOME-2 covers the spectral range between 240 and 790 nm in four detector channels. The fourth channel (590–790 nm) provides a spectral resolution of approximately 0.5 nm, a signal-to-noise ratio (SNR) up to 2000 and comprehends the SIF emission in approximately 650–800 nm as it is shown in Fig. 1. Here, we use a subset of this channel from GOME-2 on-board MetOp-A, namely the spectral region between 720 and 758 nm covering 191 spectral points, to evaluate the SIF value at the second fluorescence emission peak in 740 nm. The large default swath width of 1920 km with a footprint size of 80 km × 40 km enables a global coverage within 1.5 days. The GOME-2 level 1B product consists of radiance spectra in photons per second, whereas the spectral solar irradiance is also acquired by the measurement device. Satellite data covering the 2007–2011 time period has been available for this study.

AMTD
7, 12173–12217, 2014

2.2 SCIAMACHY

SCIAMACHY (Bovensmann et al., 1999) was one of ten instruments on-board ESA's Environmental Satellite (ENVISAT). ENVISAT was launched in March 2002 and became non-operational in April 2012, when the communication was interrupted. Similar to MetOp-A, the satellite has a sun-synchronous orbit at an altitude of approximately 800 km with an overpass time at 10:00 local solar time and one revolution around the earth takes about 100 min. The SCIAMACHY instrument was designed to measure distributions of various chemical trace gases in the atmosphere and has a similar radiometric performance as GOME-2 in the near-infrared. Overall, a spectral range of 240–2400 nm is covered by eight detector channels, whereas a subset of the fourth channel (604–805 nm, spectral resolution of 0.48 nm, SNR up to 3000) can be used to evaluate the amount of SIF at the second fluorescence emission peak in 740 nm. SCIAMACHY measured alternately in nadir and limb mode which leads to blockwise rather than continuous nadir measurements. Due to this default scan option, a global coverage is achieved within six days. The swath width of 960 km is only half as large as the swath width of GOME-2 while the spatial resolution along track is 30 km and the nominal across track pixel size is 60 km, but due to data rate limitations, radiances in the spectral range of interest were captured at 240 km (four pixels binned) across track. That means only certain spectral windows have a higher spatial resolution (e.g. inside the O_2 A-band) and original pixels are co-added on-board in most wavelength regions in order to meet the downlink limitations. Using the spectral interval between 720–758 nm to retrieve SIF leads therefore to a reduced spatial resolution by a factor of 2–3 compared to GOME-2. As stated in Lichtenberg et al. (2006), two relevant corrections have to be applied in the processing chain of the level 1 data for the considered wavelength range: the memory effect correction and the dark signal correction. The first correction is probably more critical and a potential error source in the SIF retrieval because the memory effect modifies the absolute value of the signal and it involves the risk of artificial spectral features in the measurements. Both changes produce artifacts

AMTD
7, 12173–12217, 2014

that are expected to influence SIF retrieval results since the level of SIF in comparison to the total signal at the sensor is basically low. Satellite data for January, April and July 2011 has been available for this study.

3 Retrieval methodology

3.1 Fundamental basis

The main challenge to retrieve SIF from space-borne instruments is to isolate the SIF signal from the about 100 times more intense reflected solar radiation in the measured top-of-atmosphere (TOA) radiance spectrum. This section describes a strategy which is similar to data-driven method proposed by Joiner et al. (2013).

In simplified terms, the separation of the different contributions of the TOA signal can be achieved by the modeling of the atmospheric absorption and the in-filling of solar as well as atmospheric absorption features by SIF. The TOA radiance measured by the instrument (L_{TOA}) over a Lambertian reflecting surface can be formulated as:

$$L_{\mathrm{TOA}} = I_{\mathrm{sc}} \cdot \frac{\mu_0}{\pi} \cdot \left(\rho_0 + \frac{\rho_{\mathrm{s}} \cdot T_{\downarrow\uparrow}}{1 - \rho_{\mathrm{s}} \cdot S_{\mathrm{a}}} \right) + \frac{F_{\mathrm{s}} \cdot h_{\mathrm{f}} \cdot T_{\uparrow}}{1 - \rho_{\mathrm{s}} \cdot S_{\mathrm{a}}} \quad (1)$$

where I_{sc} is the solar irradiance at the TOA, μ_0 is the cosine of the solar zenith angle, ρ_0 is the atmospheric reflectance, ρ_{s} is the surface reflectance, S_{a} is the atmospheric spherical albedo, $T_{\downarrow\uparrow}$ is the total atmospheric transmittance (in downward and upward direction), F_{s} is the amount of sun-induced fluorescence at 740 nm (second peak of the emission spectrum), h_{f} is a normalized reference fluorescence emission spectrum and $T_{\uparrow}$ is the atmospheric transmittance in the upward direction. The equation can be simplified by assuming $\rho_{\mathrm{s}} \cdot S_{\mathrm{a}} \ll 1$ as follows:

$$L_{\mathrm{TOA}} = I_{\mathrm{sc}} \cdot \frac{\mu_0}{\pi} \cdot (\rho_0 + \rho_{\mathrm{s}} \cdot T_{\downarrow\uparrow}) + F_{\mathrm{s}} \cdot h_{\mathrm{f}} \cdot T_{\uparrow} \quad (2)$$

AMTD
7, 12173–12217, 2014

As stated above, we use a statistical atmospheric modeling similar to Joiner et al. (2013) in order to separate spectral features from atmospheric absorption, apparent reflectance and SIF. A subset of the fourth channel of GOME-2 (590–790 nm with a spectral resolution of 0.5 nm and a signal-to-noise ratio up to 2000) and SCIAMACHY (604–805 nm with a spectral resolution of 0.48 nm and a signal-to-noise ratio up to 3000), namely the spectral window from 720–758 nm, is used to perform SIF retrievals. This retrieval window has been selected for the following reasons:

1. It covers the second peak of SIF emission (at 740 nm), at which we evaluate the amount of SIF.
2. It contains spectral regions with a high atmospheric transmittance (between 721.5–722.5 and 743–758 nm), which is necessary to characterize the apparent reflectance.
3. The lower limit of 720 nm has been chosen considering that an extended retrieval window requires a more complex model. Simultaneously, it is advantageous to capture a spectral region with a high transmittance at both edges of the retrieval window in order to estimate the apparent reflectance with a sufficient accuracy.
4. The upper limit of 758 nm is due to the ensuing O_2 A-band, which exhibits a stronger absorption and would potentially complicate the radiative transfer problem.

The basic idea of the statistically based approach is that spectra without SIF emission can be used to reproduce the variance of the transmission through the atmosphere also for spectra which contain SIF. For this purpose, the data is divided into a training and a test set as described below.

3.2 Selection of training and test sets

The selection of the training set is highly relevant to obtain meaningful results because this data will be used to model the transmittance of the actually desired measurements.

AMTD
7, 12173–12217, 2014

It is therefore essential to capture as many atmospheric states as possible within the training set. Random samples of measurements over areas where no SIF signal is expected (e.g. deserts, ice, sea and thick clouds) are used for this purpose. The selection of such measurements is based on the determination of the land cover using the International Geosphere and Biosphere Programme (IGBP) classification (Friedl et al., 2002) derived from MODIS data. Care is taken to ensure that only homogeneous, non-vegetated land cover classes serve as a basis for the training set. Furthermore, it has to be noted that the training set is sampled on a daily basis.

Cloud contamination of measurements is problematic for the test set since it can be expected that the SIF signal is partly absorbed in the presence of clouds, which potentially biases the retrieval. For this reason, the range of cloud fractions is limited which saves also computation time, whereas the restriction is explicitly not applied to the training set. We use the effective cloud fraction from the Fast Retrieval Scheme for Clouds from the O_2 A-band (FRESCO, Wang et al., 2008). In the case of GOME-2, the provided cloud fraction is already attached to the level 1B satellite data. The FRESCO cloud fraction data for SCIAMACHY was available separately and had to be collocated with the satellite data.

In general, the test set is composed of all available land pixels with a cloud fraction below 0.5 or an unknown cloud fraction. The FRESCO cloud fraction is namely not available for the presence of snow, ice or sun-glint, which is of particular relevance in the winter time at higher latitudes. In order to obtain a complete time series of SIF in regions with snow coverage, we evaluate also measurements with an unknown cloud fraction. The reason for using the certain threshold of 0.5 will be discussed in Sect. 5.5.

3.3 Preparation of training set and generation of atmospheric principal components

The training set is used to model the transmission of the test set containing the targeted SIF. Therefore, a Principal Component Analysis (PCA) is applied to the estimated transmissions of the training set in order to obtain atmospheric principal components (PCs).

AMTD
7, 12173–12217, 2014

Actually, these PCs and not the original training set are then utilized to model the transmission of the test set. First of all, it is necessary to estimate the transmissions of the training set as described below.

Because the second summand from Eq. (2) is zero for any SIF-free spectrum, the transmission can be assessed through the TOA reflectance. The TOA reflectance is obtained through the normalization of a spectrum by the solar irradiance (I_{sc}) (which is also measured by GOME-2/SCIAMACHY), the cosine of the solar zenith angle (μ_0) and π. Such a sample TOA reflectance spectrum measured by GOME-2 is shown in Fig. 2. We assume two windows devoid of atmospheric absorption within the retrieval window, namely the spectral regions between 721.5–722.5 and 743–758 nm, in order to estimate the apparent reflectance by a third order polynomial (also shown in Fig. 2). Since the signal in the assumed atmospheric windows originates not only from the actual surface reflectance, but also from the atmosphere itself (atmospheric path radiance), it must be noted that this is not exclusively an estimation of the surface reflectance, but rather of the apparent reflectance.

Vegetation has a unique, spectrally smooth reflectance signature in the considered wavelength range, which means that there are no distinct absorption lines. Nevertheless, the spectral reflectance of vegetated areas changes rapidly in the red edge region (680–730 nm) which is due to the different spectral absorption by chlorophyll. Using the narrow atmospheric window at 722 nm assures that the apparent reflectance can be modelled in a sufficient precision for the part of the retrieval window which is affected by the red edge. Extending the retrieval window to lower wavelengths would lead to errors in the reflectance estimation caused by a lack of further atmospheric windows (the next spectral region with a high atmospheric transmittance is located at wavelengths below 710 nm). This error translates into the transmittance estimation which would propagate to errors in SIF. Extending the retrieval window to the O_2 A-band at 760 nm would be possible and has also been shown by Joiner et al. (2013), but a benefit cannot be expected. As already stated by Frankenberg et al. (2011a), the separation from SIF and atmospheric scattering properties is ambiguous when using only O_2 absorption lines.

AMTD
7, 12173–12217, 2014

Also Joiner et al. (2013) reported that a removal of the O_2 A-band is not accompanied with a significant loss of information content. On the other hand, it is possible to confine the retrieval window, whereby a loss of information content regarding SIF is expected, which potentially leads to a loss of retrieval precision. A benefit from a smaller retrieval window would be a lower number of required PCs associated with decreased computation times.

Figure 2 depicts a third order polynomial fit in the assumed atmospheric windows, which is performed in order to estimate the apparent reflectance.

This estimate is then used to obtain transmission spectra (e.g. Fig. 3) from the training set. As Joiner et al. (2013) we use a PCA to convert SIF free transmission spectra (training set) into a set of linearly uncorrelated variables, which can be used to reconstruct each SIF free spectrum in an appropriate precision only by a subset of PCs. As already mentioned in Sect. 3.2, it is necessary to capture a sufficient number of atmospheric states within the training set so that the transmission spectra of the test data can also be adequately constructed by the PCs. An important advantage using this method is that there is no need to perform explicit radiative transfer simulations to characterize atmospheric parameters which affect the measurement (e.g. temperature and water vapour profiles). Instrumental artifacts and degradation are also captured by this method and do not need to be considered.

3.4 Forward model

Through the estimation of the apparent reflectance (by a third order polynomial) and the transmission of the atmosphere (by a subset of PCs) the final forward operator results in:

$$\boldsymbol{L}_{\mathrm{TOA}} = \boldsymbol{I}_{\mathrm{sc}} \cdot \frac{\mu_0}{\pi} \cdot \sum_i (\alpha_i \cdot \boldsymbol{\lambda}^i) \cdot \sum_j (\beta_j \cdot \boldsymbol{PC}_j) + F_{\mathrm{s}} \cdot \boldsymbol{h}_{\mathrm{f}} \cdot \boldsymbol{T}_{\uparrow}, \tag{3}$$

where α_i, β_j and F_{s} are the unknowns which are necessary to generate a synthetic measurement. In contrast to the previous work of Joiner et al. (2013) our forward model

AMTD
7, 12173–12217, 2014

to describe the measurement can be solved without iterations by applying a previous step. In general, the estimation problem is inherently non-linear and can be solved by a linearization, either at each step of an iterative algorithm (Joiner et al., 2013) or in advance. We linearize the problem by estimating the upward transmission ($T_{\uparrow}$) before applying the actual forward model and thus the forward model itself becomes linear. The atmospheric transmission in the upward direction ($T_{\uparrow}$) can be roughly estimated using following formula, which expresses $T_{\uparrow}$ in terms of $T_{\downarrow\uparrow}$:

$$T_{\uparrow} = \exp\left[\ln(T_{\downarrow\uparrow}) \cdot \frac{\sec(\theta_v)}{\sec(\theta_v) + \sec(\theta_0)}\right], \quad (4)$$

where θ_v is the viewing zenith angle and θ_0 is the solar zenith angle. This means, that an estimate of the total transmission ($T_{\downarrow\uparrow}$) is firstly required. For this purpose, each measurement is normalized in the same way as for the training set, which includes that we assume that F_s is zero, although these measurements potentially contain a SIF emission. The TOA reflectance is then normalized by the estimated apparent reflectance obtained by a third order polynomial fit in non-absorbing wavelengths (two atmospheric windows shown in Fig. 2).

Figure 3 depicts such a resulting transmission in the upward direction ($T_{\uparrow}$). It must be noted that the resulting estimate of $T_{\downarrow\uparrow}$ through the normalization is not sufficient for the actual retrieval (Eq. 3) because the SIF signal is still part of the spectra (if a fluorescent target is observed). The only purpose of this step is to obtain an appropriate estimate of $T_{\uparrow}$, as this factor only modifies the spectral shape of the SIF emission. Within the retrieval $T_{\downarrow\uparrow}$ is modelled by the PCs, which were obtained exclusively from spectra without SIF, and the β_j coefficients.

3.5 Backward elimination algorithm

From a theoretical point of view, there is no reason to prefer an unnecessarily complex model rather than a simple one. To account for this fact, we use a backward elimination algorithm in addition to the previously presented steps to reduce the number of

AMTD
7, 12173–12217, 2014

coefficients to fit. The forward model in Eq. (3) contains $i \cdot j + 1$ (α_i, β_j, F_s) coefficients to fit, whereas not all of these coefficients are necessarily required. Joiner et al. (2013) reported that only a few PCs can explain already a very large amount of variance (> 99.999 %) of the normalized radiance. Using too many PCs and thus coefficients to fit might therefore result in an overfitting of the measurement. For this reason, we start with all candidate variables and remove each variable despite of variables for the first PC (carrying the most variance) and the targeted SIF in order to test if any removal improves the model fit to the data. The candidate variables, which are individually removed, can be seen more obvious if the part from Eq. (3) containing the $i \cdot j$ coefficients is summarised as follows:

$$\sum_i (\alpha_i \cdot \boldsymbol{\lambda}^i) \cdot \sum_j (\beta_j \cdot \boldsymbol{PC}_j) = \sum_{i,j} (\gamma_{i,j} \cdot \boldsymbol{\lambda}^i \cdot \boldsymbol{PC}_j), \quad (5)$$

where i is ranging from 0–3 (third order polynomial fit to estimate the apparent reflectance) and j is ranging from two to the desired number of provided PCs. If any removal improves the model fit to the data, the removed variable, which improves the model fit the most, is abandoned in the state vector from the forward model in Eq. (3). This process is repeated until no further improvement occurs (for each single retrieval). The improvement is determined through the Bayesian information criterion (BIC, Schwarz, 1978), which is in simplified terms the goodness of fit weighted by the number of coefficients. The BIC is used as a statistical tool for model selection and balances the goodness of fit with the model complexity, whereas complexity refers to the number of parameters in the model.

Using the backward elimination algorithm has the consequence that the number of provided PCs is unimportant, as long as there are more PCs provided than actually necessary for an appropriate fit. In reverse it means that the optimum number of PCs is determined automatically. The detailed behaviour of this supplementary step in comparison to a simple linear regression using all potential coefficients (all candidate variables) will be shown below in Sect. 4.3.

AMTD
7, 12173–12217, 2014

3.6 Uncertainty estimation

In order to assess the uncertainty of the SIF measurements, the 1σ retrieval error is calculated by propagating the measurement noise. We assume that measurement noise can be characterized by spectrally-uncorrelated Gaussian noise. In this case, following Sanders and de Haan (2013), the signal-to-noise ratio (SNR) can be calculated for any radiance level if the SNR is known for a reference radiance level L_{ref} at a reference wavelength λ_i^{ref} following:

$$\text{SNR}(\lambda_i) = \text{SNR}_{\text{ref}} \cdot \sqrt{\frac{L(\lambda_i)}{L_{\text{ref}}}}. \quad (6)$$

Here, we propagated the measurement error of GOME-2 using calculations of the SNR vs. level 1B calibrated radiances (averaged from 757.7–758 nm) under defined conditions (2 % albedo, solar zenith angle of 0°, integration time of 1.5 s) performed by EUMETSAT. The error is then calculated through the evaluation of the retrieval error covariance matrix given by:

$$\mathbf{S_e} = \left(\mathbf{K}^{\mathrm{T}}\mathbf{S_0}^{-1}\mathbf{K}\right)^{-1}, \quad (7)$$

where $\mathbf{K}$ is the Jacobian matrix formed by linear model parameters from Eq. (3) and $\mathbf{S_0}$ is the measurement error covariance matrix, which is a diagonal matrix (because of the assumption of spectrally-uncorrelated noise) with the elements:

$$\sigma_i^2 = \left(\frac{L(\lambda_i)}{\text{SNR}(\lambda_i)}\right)^2. \quad (8)$$

Furthermore, the standard deviation (SD) from monthly mapped SIF has been computed for SCIAMACHY and GOME-2 as follows:

$$\text{SD}_{\overline{F_s}} = \frac{\sigma}{\sqrt{n}}, \quad (9)$$

AMTD
7, 12173–12217, 2014

where σ is the SD and n is the number of observations per grid cell in order to assess the uncertainty in the mean. This value is a measure of instrumental noise plus natural variability of SIF in the considered time range.

3.7 Quality control

Since it can not be excluded that the retrieval fails for single measurements, the retrieval results have to be checked. This is done by using the residual sum of squares (RSS) from each retrieval. The resulting coefficients are used to generate a synthetic measurement which is compared with the original measurement. The RSS value is then the discrepancy between the data and the model. One major issue which causes high residuals is the South Atlantic Anomaly (SAA) which will be discussed below in Sect. 5.3. In general, it appears that the RSS value is around $0.5\,(\mathrm{mW\,m^{-2}\,sr^{-1}\,nm^{-1}})^2$. Single retrievals are removed if the RSS is above $2\,(\mathrm{mW\,m^{-2}\,sr^{-1}\,nm^{-1}})^2$ for both GOME-2 and SCIAMACHY. It turned out, that monthly composites from GOME-2 SIF retrieval results contain striping effects from single swaths in individual cases. This issue might be caused by special orbits (e.g. narrow swath) and is solved by removing distinct swaths with a high average of RSS values. This striping effect was not yet observed for SIF results obtained from SCIAMACHY at this preliminary stage. A further filtering beside the residual check is not required.

4 Sensitivity analysis

The retrieval has been tested for a wide range of conditions using simulated radiances in order to assess retrieval precision and accuracy as well as the effect of the backward elimination algorithm. This section describes the underlying simulations briefly and examines retrieval properties and advantages with respect to a simple linear model without a backward elimination.

AMTD
7, 12173–12217, 2014

4.1 Simulated TOA radiances

Similar to Joiner et al. (2013), we use simulated sun-normalized TOA radiances from the Matrix Operator MOdel (MOMO) radiative transfer code (Fell and Fischer, 2001) with a spectral sampling of 0.005 nm. These simulations comprehend two viewing zenith angles (0, 16°), four solar zenith angles (15, 30, 45, 70°), two atmospheric temperature profiles (middle latitude summer and winter), four surface pressures (955, 980, 1005, 1030 hPa), four water vapour columns (0.5, 1.5, 2.5, 4.0 cm), three aerosol layer heights (500–700, 600–800, 700–900 hPa) using a continental aerosol model and five aerosol optical thicknesses at 550 nm (0.05, 0.12, 0.2, 0.3, 0.4). Apart from the observation and illumination geometry, simulations for 480 different atmospheric states have been carried out in order to test the retrieval. In this case, the training set uses a spectral library of 10 different soil and snow surface reflectance spectra, which means that the training data contains 38 400 samples. A set of top-of-canopy (TOC) reflectances and SIF spectra derived with the FluorSAIL radiative transfer model has been utilized to produce the test data set. The surface reflectance is thereby a function of chlorophyll content and Leaf Area Index (LAI), while SIF is a function of chlorophyll content (5, 10, 20, 40 $\mu g\,cm^{-2}$), LAI (0.5, 1, 2, 3, 4 $m^2\,m^{-2}$) and quantum efficiency (which affects the intensity of the SIF flux; 0.02, 0.05, 0.08). It follows from these 60 diverse TOC fluorescence spectra and various simulations that the test data is composed out of 230 400 samples. We convolve the high spectral resolution TOA spectra (0.005 nm) to a lower resolution spectrometer grid with a 0.5 nm full-width at half-maximum and a spectral sampling interval of 0.2 nm which is similar to GOME-2 and SCIAMACHY. A realistic instrumental noise with respect to the calculated SNR from GOME-2 (in relation to the radiance level at a reference wavelength) provided by EUMETSAT is then added to the spectra using Eq. (6).

AMTD
7, 12173–12217, 2014

4.2 End-to-end simulation

Figure 4 depicts the result of the end-to-end simulation using the retrieval window ranging from 720–758 nm and providing the first eight PCs derived from the training set. The mean and SD of the 480 simulated atmospheric states as well as the illumination and observation angles were calculated for each of the 60 TOCs.

In view of the good correspondence between input and retrieved SIF in the end-to-end simulation, it can be stated that the retrieval method is appropriate for the separation of the SIF signal from the TOA radiance.

One limitation of this sensitivity study consists in the absence of clouds, which impact the retrieval of SIF inevitably. The result of other simulation studies by Frankenberg et al. (2012) and Guanter et al. (2014b) suggests that an underestimation of SIF can be expected in the presence of clouds. The reason is a decrease in atmospheric transmittance through clouds which is not captured by the forward model. Nevertheless, this should be of secondary importance when evaluating the pure retrieval methodology. Furthermore, we will assess the impact of clouds on the retrieval based on real satellite measurements in Sect. 5.5.

4.3 Influence of number of PCs used and backward elimination

We performed the retrieval several times using 5–25 PCs in order to assess the sensitivity to the number of provided PCs. In addition, the backward elimination algorithm was disabled (all $i \cdot j + 1$ coefficients from Eq. (3) are used) to evaluate whether the algorithm is capable to reduce the noise and avoid an overfitting. Results are presented in Fig. 5 in form of various statistical comparisons which are evaluated and described below.

The bias which was calculated through the mean difference of retrieved minus input SIF represents the accuracy of the retrieval. It can be seen that the bias drops down to a value close to zero when using/providing more than seven PCs for both the linear model fit (using all coefficients) and the backward elimination fit (using only selected

AMTD
7, 12173–12217, 2014

coefficients). Using all coefficients leads to a slightly increasing bias associated with a larger number of PCs, which is not the case when the backward elimination is applied. The correlation between retrieved and input SIF is close to one when eight or more PCs are used/provided.

The root-mean-square error (RMSE), which is a measure of the differences between the input and retrieved SIF values, shows also an almost stable behaviour associated with low values when using/providing more than seven PCs. RMSE values derived from simulations using all coefficients are slightly lower but increase with an increased usage of PCs up to the level of the backward elimination model.

A significant difference between the disabled and enabled backward elimination algorithm is firstly visible in the comparison of the mean SD of the retrieval which represents the precision of the retrieval. The SD of retrieved SIF values using the backward elimination fit remains constantly low (when providing more than seven PCs), while the SD increases for the linear model fit with a larger number of PCs.

Even more pronounced differences arise in the comparison between the mean Bayesian information criterion (BIC) values. This fact is expected since the number of coefficients serves as weight for this criterion (as described in Sect. 3.5). For an interpretation of the BIC it has to be noted that the model with the lowest value is to be preferred. As a consequence, the BIC can be used to determine the appropriate number of PCs for the retrieval. It turns out that six to eight PCs should be used for the linear model fit using all coefficients, while at least eight PCs should be provided for the backward elimination fit. This finding concurs with the results from the previous comparisons and supports the applicability of this criterion. It has to be mentioned that the order of magnitude of BIC values clearly shows that the backward elimination fit should be preferred in any case. A potential overfitting of the measurement can be successfully prevented in this way.

As in Fig. 4, a linear fit of TOC means was made for the retrievals with an increasing number of PCs. Intercepts and slopes of these fits are depicted in the last two plots of Fig. 5, whereas values should be zero and one for ideal retrievals. Slightly differing

AMTD
7, 12173–12217, 2014

results from the ideal case occur only in intercept values where the backward elimination algorithm performs better.

Even if differences are small, it can be concluded that the precision is enhanced (decreased SD) if the backward elimination is enabled. This means that noise is reduced by selecting only appropriate coefficients which is expected to be of particular importance for real satellite measurements. Unfortunately, there is no ground truth against which the retrieval could be adjusted or validated under real-life conditions. As a consequence, it is not possible to determine the most appropriate number of PCs for real satellite data. Thus, it is advantageous that the backward elimination algorithm ensures stable results, regardless how many PCs are provided (with the restriction that there is a minimum number of required PCs). Furthermore, an overfitting of the measurement is avoided by using the discussed algorithm. As a conclusion of these findings, we decided to provide 10 PCs for the retrieval applied to real GOME-2 and SCIAMACHY data. The backward elimination algorithm selects the required model parameters (a subset of candidate variables from Eq. 5) based on the BIC for each pixel automatically.

We performed this extensive simulation study for additional retrieval windows (710–758, 715–758, 725–758, 730–758, 735–758 nm) with the result that confined retrieval windows lead to a slight bias while extended retrieval windows require the use of a larger number of PCs. In terms of computation time and retrieval accuracy the selected retrieval window from 720–758 nm is therefore reasonable.

5 Results

The presented SIF retrieval method has been used to produce a global SIF data set from GOME-2 data covering the 2007–2011 time period. In addition, the SIF retrieval has been implemented on a trial basis for SCIAMACHY data in January, April and July 2011. This section describes results from monthly composites as well as a comparison to the results from Joiner et al. (2013). We also discuss an important limitation which

AMTD
7, 12173–12217, 2014

arises due to the South Atlantic Anomaly (SAA). Furthermore, the impact of clouds on the retrieval will be assessed.

5.1 Monthly composites

In general, it is possible to achieve a global coverage of SIF measurements within 1.5 days (for GOME-2) but the presence of clouds prevents such a high temporal resolution. In practice, the temporal resolution for global data coverage should amount at least eight days. Although it is important to consider different time scales, it is common to produce monthly means. Two monthly composites of SIF in January and July 2011 derived from SCIAMACHY and GOME-2 data are shown together with GOME-2 SIF results provided by Joiner et al. (2013) in Fig. 6.

Overall all three results compare very well concerning spatial patterns, although the SIF composite derived with SCIAMACHY is provided in a spatial resolution of $1.5^\circ \times 1.5^\circ$, whereas SIF retrievals from GOME-2 are rastered in $0.5^\circ \times 0.5^\circ$ grid boxes. The lower spatial resolution for SCIAMACHY is due to the fact that the original pixels are co-added in certain wavelength regions in order to meet downlink limitations. Absolute SIF values obtained from SCIAMACHY are slightly lower than from GOME-2. One reason might be a higher cloud contamination of the bigger footprints from SCIAMACHY. As already stated in Sect. 4.2, simulation studies by Frankenberg et al. (2012) and Guanter et al. (2014b) have shown that an underestimation of SIF caused by clouds can be expected. In order to test the reasonable thesis that lower SCIAMACHY SIF values are caused by a higher cloud contamination, we derived the normalized difference vegetation index (NDVI, Tucker, 1979) as a reference. We calculate the NDVI from the spectral reflectance acquired in two bands (red, near-infrared) as follows:

$$\mathrm{NDVI} = \frac{\rho_{\mathrm{NIR}} - \rho_{\mathrm{red}}}{\rho_{\mathrm{NIR}} + \rho_{\mathrm{red}}}, \tag{10}$$

where ρ_{NIR} is the mean radiance between 780–785 nm and ρ_{red} is the mean radiance between 660–665 nm. Following Guanter et al. (2014b), it is expected that the

AMTD
7, 12173–12217, 2014

impact of clouds on the NDVI is more pronounced than on SIF retrievals. Since the NDVI is derived by a simple ratio of two spectral bands, results are unaffected from general retrieval properties (in the case of the presented SIF retrieval: different solar irradiance measurements, training sets, atmospheric PCs and quality filtering). It has to be emphasized that the NDVI always decreases with an increasing cloud fraction. Thus, a lower NDVI would indicate either a higher cloud contamination or radiometric problems. A supplementary comparison of NDVI values obtained from GOME-2 and SCIAMACHY is therefore appropriate to investigate if the thesis that a higher cloud contamination of SCIAMACHY pixels leads to lower SIF values can be supported. Hence, two scatter plots between SIF and NDVI, respectively, using GOME-2 and SCIAMACHY data are shown in Fig. 7. It has to be considered that this comparison uses only measurements from vegetated pixels (using the IGBP land cover classification) with cloud fractions below 0.5. As it can be seen in Fig. 7, there is an unbiased relationship between NDVI results, while SIF results show a slightly low-biased linear relationship (slightly lower SCIAMACHY SIF values). It must therefore be concluded that the reason for lower SCIAMACHY SIF values is most likely not associated with a higher cloud contamination of SCIAMACHY footprints. Another possible explanation for the low-biased relationship could be found in different solar irradiance measurements or it could be even more complex. Nevertheless it can be concluded that data from both GOME-2 and SCIAMACHY can be used to obtain comparable NDVI and SIF values. It must be noted that the SIF results derived from SCIAMACHY data are scaled in Fig. 6 by the relationship found in Fig. 7 in order to ensure a visual comparability.

The high SIF average in January 2011 in South America must be treated with caution, because this region is particularly affected by the South Atlantic Anomaly. This limitation will be discussed in Sect. 5.3 but it should already be considered at this point to avoid a misinterpretation. It is noticeable that the border between areas with moderate SIF values and areas with low SIF values in Australia are more defined for the SIF composite derived with SCIAMACHY data. This fact suggests a lower noise level of SCIAMACHY SIF retrievals at least in the considered region, which is probably

AMTD
7, 12173–12217, 2014

due to the spatial averaging. That means the noise is reduced because more photons are binned per observation. SIF values on the Northern Hemisphere are close to zero which is expected due to the vegetational inactive period. The appearance of the map changes fundamentally for July. It is interesting to note the high SIF average in the US Corn Belt region with respect to other regions at the same latitude, which is produced by large crop- and grassland areas. This region with pronounced SIF averages was examined in detail by Guanter et al. (2014a) with the finding, that SIF provides a direct measure of gross primary production (GPP) in cropland and grassland ecosystems. Furthermore, it has been stated that current carbon cycle models severely underestimate the GPP in such regions. As expected, regions with none or sparse vegetation show low SIF values in both evaluated months.

The standard error of the mean derived with GOME-2 for July 2011 is shown in Fig. 8 in order to provide an exemplary estimate of the overall uncertainty of monthly SIF composites. The standard error of the mean is calculated for each grid cell by:

$$\sigma^2(\overline{F_s}) = \frac{1}{\sum_{i=1}^{n}(1/\sigma_i)}, \tag{11}$$

where $\overline{F_s}$ is the mean SIF value, and σ_i is the 1σ retrieval error given by Eq. (7). It represents the instrumental noise weighted by the number of observations per cell. Highest uncertainties occur over bright areas associated with a higher photon noise, e.g. deserts and regions with snow/ice, as it can be seen in Fig. 8. The resulting pattern can therefore be interpreted as an error increasing with TOA radiance.

5.2 Comparison with results from Joiner et al. (2013)

As we take advantage of the basic assumptions of the proposed SIF retrieval by Joiner et al. (2013), it is reasonable to compare both results. It should be noted that there are two released versions of GOME-2 SIF (V14 & V25), whereas this comparison focusses on the latest version (V25). Main changes from V14 to V25 lie in a confined retrieval

AMTD
7, 12173–12217, 2014

window (734–758) and subsequently in a reduced number of used PCs (V14: 25 PCs, V25: 12 PCs). Furthermore, the spectra are normalized with respect to earth spectra instead of the GOME-2 solar spectra in V25. Similar to Fig. 7, a scatter plot between the V25 data set and SIF values derived with the presented algorithm is depicted in Fig. 9 for July 2011. It is immediately noticeable that the amount of SIF obtained from the presented retrieval is much higher, but there is a clear linear relationship between the two data sets. This relationship has been used to scale the monthly composites in Fig. 6 to ensure a visual comparability.

In order to compare the results more in detail, we collocated the retrieval output and produced biome specific time series. The biomes were again determined through the IGBP land cover classification (Friedl et al., 2002). Three biomes have been selected to examine similarities and differences, whereas no scaling was applied.

Firstly, evergreen needleleaf forest areas inside of a large box on the Northern Hemisphere (0–180° E, 45–75° N) are used as a basis for comparison. The resulting time series is depicted in Fig. 10 and shows the robustness of the seasonal cycle derived with both retrievals. However, the amount of SIF obtained from the presented retrieval is much higher. This discrepance increased with respect to SIF results from the older version V14 (not shown). At this point, we are not able to judge which amount of SIF is closer to reality, since there is a lack of ground truth and validation. Considering that the number of collocated measurements during wintertime is very limited, those results should not be evaluated in this comparison. It has to be mentioned that the lack of available collocated measurements is probably due to the different cloud and quality filtering, which is more restrictive for the data provided by Joiner et al. (2013). Also conspicuous is that the SD or fluctuation is continuously lower for SIF retrieved with the presented method. The SD of the V25 data exceeds the averaged SIF values in all time steps. There is no yearly variation of SIF maxima observable for the data from Joiner et al. (2013), whereas 2010 and 2011 have slightly lower yearly maxima than the 2007–2009 time period using the introduced method.

AMTD
7, 12173–12217, 2014

The second examined region is located in the US Corn Belt region (100–80° W and 35–50° N) and contains only measurements over croplands. As for the first region, it can be seen that the temporal SIF pattern is congruent for both retrievals. Even in this region, there is an obvious discrepance in absolute SIF values, whereas the difference is less pronounced than in the evergreen needleleaf forest time series. It is remarkable that the SD (or fluctuation) of the SIF data set from Joiner et al. (2013) is slightly lower than using the new data set during the vegetational active period. Since it is assumed that the examined region is mostly homogenous, it can be presumed that the results from Joiner et al. (2013) are more credible for the selected region and subsequently for the evaluated biome (croplands). This effect is reversed during the winter time which suggests that the introduced SIF retrieval is less affected by background noise.

The last examined region lies in the Sahara between 20° W–35° E and 15–35° N. This region has been selected in order to assess the noise level of the retrievals as SIF values are expected to be close to zero in non vegetated areas. Overall, both time series indicate a slight offset from the expected value close to zero. It has to be considered that such high reflective surfaces are also associated with high errors as it can be seen in Fig. 8. Hence, the obtained values are within the uncertainty range. A slight trend of SIF values can be observed in the data set of Joiner et al. (2013). On the contrary, there is no trend to be seen in the SIF retrieval results using this new method. More significant differences arise when the SD is considered. It is becoming apparent that fluctuations of the new method are only half as large.

In view of these results it can be assumed that the presented GOME-2 SIF retrieval is less affected by noise than that from Joiner et al. (2013). Beside the different algorithms, this can also be expected from the fact that our retrieval window (720–758 nm) is larger than that of Joiner et al. (2013) (734–758 nm). In general, spatio-temporal patterns compare very well as it can be seen in Fig. 6 but nevertheless, it remains unclear which values are more accurate.

AMTD
7, 12173–12217, 2014

5.3 South Atlantic Anomaly

Another point to be considered is that the error estimation might be too optimistic for large parts on the South American continent. The reason is the South Atlantic Anomaly (SAA) which is basically a regional reduced strength in the Earth's magnetic field. Hence, orbiting satellites are exposed to an increased flux of energetic particles which leads to additive noise in the measurements. An impact of the SAA on the SIF retrieval using GOME-2 data has also been described in the study of Joiner et al. (2013). Here, we depict the SD divided by the square root of the number of observations per grid cell (Eq. 9) of monthly SIF composites for January and July 2011 from our SIF retrieval using GOME-2 and SCIAMACHY data in Fig. 11 to illustrate the impact of the SAA. This comparison provides also an estimate of the uncertainty in the mean, whereas instrumental noise and natural variability are covered. The underlying SCIAMACHY SIF values to produce Fig. 11 are also scaled by the linear relationship found in Fig. 7 and both composites are computed in a spatial resolution of $1.5^\circ \times 1.5^\circ$ in order ensure a comparability.

The center of the SAA is in close proximity to the coast of Brazil at about 40° W and 30° S which results in extraordinary high SDs for the GOME-2 SIF data set in nearby regions. Overall, higher SDs occur where a significant amount of SIF can be observed (see Fig. 6). It can also be seen that the SD is generally lower for the GOME-2 SIF composites (except for the SAA affected regions), which is due to a better spatial sampling. It is remarkable that the SAA seems to have a much lower impact on measurements performed by SCIAMACHY in particular for July 2011, although the difference in orbit height is only about 20 km. In view of Fig. 11 it is even questionable whether there is an impact of the SAA on SCIAMACHY data at all.

In contrast to the SCIAMACHY data set, the impact of the SAA on GOME-2 data translates also to the residual sum of squares of the SIF retrieval (not shown). High RSS values occur in particular in the region of large SDs on the South American continent. This allows the conclusion that the noise and thus the measurement error is much

AMTD
7, 12173–12217, 2014

higher than expected from our error propagation depicted in Fig. 8. Although all single retrievals with an RSS bigger than 2 $(\mathrm{mW\,m^{-2}\,sr^{-1}\,nm^{-1}})^2$ are filtered, care should be taken when using SIF retrieval results from affected areas, especially for GOME-2 SIF retrievals.

5.4 North–south bias in training set

Consistency checks and plausibility controls of the derived SIF values have lead to another source of error. We retrieved SIF values from the training set (sea, desert and ice) with the expectation that all SIF values are close to zero. It turned out that there is a slight time- and latitude-dependent offset in retrieved SIF values which amounts up to 0.3 $\mathrm{mW\,m^{-2}\,sr^{-1}\,nm^{-1}}$ for GOME-2 SIF results. Figure 12 depicts the monthly composite of SIF of the training set averaged over latitudes derived from GOME-2 and SCIAMACHY data for July 2011. As it can be seen, there is no offset observable when SCIAMACHY data is used, which supports the thesis that this bias is related to an instrumental issue. One reason might be a temperature-dependent dark current change. Since it would be difficult to correct for this kind of bias and due to its slightness, we decided to preliminarily neglect it. Nevertheless, this issue should be considered in further investigations.

5.5 Impact of clouds on the retrieval

In contrast to the usually applied pre-filtering of cloud contaminated measurements (discussed in Sect. 3.2), we run the retrieval using GOME-2 data in 2009 without restricted cloud fractions in order to examine the impact of clouds.

Tropical rainforest areas are frequently covered by clouds and therefore, it is expected that clouds may effect the retrieval of SIF in particular in such regions. Therefore, we produced a time series over a box in the Amazon Basin (70–65° W, 5–0° S, covered with evergreen broadleaf forest) using different cloud fraction thresholds which is shown in Fig. 13. Care was taken when selecting the area to ensure that the impact

AMTD
7, 12173–12217, 2014

of the SAA is as low as possible and the IGBP land cover (Friedl et al., 2002) (evergreen broadleaf forest) is most homogenous.

Overall it can be seen that SIF values are decreasing with an increasing cloud fraction threshold, whereby the temporal pattern remains almost unaffected. Using only retrievals with a low cloud fraction (< 0.25) implies a significant loss of measurements while the SD (or fluctuation) is only slightly smaller and even equal for some time steps. SIF values are successively decreasing by relaxing the threshold which is consistent with the expectation that the SIF signal is partly absorbed by clouds. An exception occurs in one time step where the reported SD is significantly higher than in the other time steps. Simultaneously, the number of included retrievals is low and differences in cloud fraction values from FRESCO are only marginal. For these reasons, the time step at the end of October 2009 is not meaningful to evaluate the impact of clouds on the retrieval. Applying a cloud fraction threshold of 0.5 results in differences about $0.1\,\mathrm{mW\,m^{-2}\,sr^{-1}\,nm^{-1}}$ in comparison to the SIF averages of the lowest evaluated cloud fraction. The highest increase of measurements with respect to a cloud fraction threshold of 0.25 can be achieved by using measurements with cloud fractions up to 0.5. A further increase of the cloud fraction has the consequence that more measurements can be used but the amount of SIF averages is distinctly decreasing. It must be noted that results remain consistent for different spatio-temporal scales and the presented region has been chosen as a representative example. On this basis, a cloud fraction threshold of 0.5 is a reasonable compromise between the loss of measurements and changes in the SIF average. The FRESCO cloud fraction is not available for the presence of snow and ice, which is of particular relevance to the time series in winter time at higher latitudes. Including also the unknown cloud fractions in the time series of Fig. 13 has almost no impact (not shown), but allows to retrieve also SIF values in presence of ice and snow which are basically close to zero. As a consequence, we provide the global SIF data set covering the 2007–2011 time period for measurements with cloud fractions lower than 0.5 including also measurements with unknown cloud

AMTD
7, 12173–12217, 2014

fractions. Nevertheless, in view of these results it can be concluded that the presented SIF retrieval method is robust against cloud contamination.

6 Conclusions

A new approach to retrieve SIF from GOME-2 and SCIAMACHY data has been introduced in this contribution. We have presented a continuous SIF data set covering the 2007–2011 time period using GOME-2 data. Furthermore, we have been able to demonstrate that this new approach is also applicable to SCIAMACHY data, which represents the first SIF retrieval at 740 nm from SCIAMACHY in the literature.

We use a statistically based approach similar to Joiner et al. (2013) to separate spectral features from atmospheric absorption, surface reflectivity and SIF. The main idea is thereby to use a PCA to convert SIF free spectra (training set) into a set of linearly uncorrelated variables, which can in turn be used to model the atmospheric transmission of the test data including SIF. In contrast to Joiner et al. (2013) our forward model is linear, allowing to apply a backward elimination algorithm in order to reduce the number of coefficients to fit. The main benefit thereby is that the number of necessary PCs is determined automatically. The underlying assumption to achieve a linear model is that the upward transmission can be estimated before applying the actual forward model. We performed an extensive sensitivity study to explore retrieval properties and advantages using the backward elimination algorithm. As a result it can be noted that the precision is enhanced, retrieval noise is reduced and the risk of overfitting is minimized.

A discrepance in absolute SIF values arises when comparing the retrieval results with results from Joiner et al. (2013) (V25), although spatio-temporal patterns are similar. It remains exceedingly difficult at present to judge which values are more accurate. Furthermore, it must be considered that the SAA causes high uncertainties in large parts of the South American continent when using GOME-2 data. In contrast, a significant impact of the SAA on SCIAMACHY data has not been found. Although the achievable spatial resolution of SIF maps from SCIAMACHY data is coarser than from

AMTD
7, 12173–12217, 2014

GOME-2, it might be worthwhile to produce a continuous SIF time series from SCIAMACHY as well, which would extend the available SIF data sets for an additional period of four more years back to 2003. This would lead to a more than a decade long record of SIF.

On the basis of the GOME-2 SIF data set in 2009, we have shown that the retrieval is barely affected by cloud contamination. It has essentially been found that the SIF signal decreases slightly with an increasing cloud fraction.

Finally, it has to be noted that the flexibility of the retrieval method makes it also applicable to other instruments with a similar spectral and radiometric performance as GOME-2 and SCIAMACHY, such as the upcoming TROPOMI on board the Sentinel-5 Precursor and the FLEX Earth Explorer 8 candidate mission.

Acknowledgements. The research is funded by the Emmy Noether Programme of the German Research Foundation. With thanks to EUMETSAT to make the GOME-2 data available and ESA for providing the SCIAMACHY data. Jochem Verrelst and Luis Alonso from the University of Valencia are gratefully thanked for the reflectance and fluorescence simulations produced in the framework of the ESA FLUSS project.

References

Bovensmann, H., Burrows, J., Buchwitz, M., Frerick, J., Noël, S., Rozanov, V., Chance, K., and Goede, A.: SCIAMACHY: mission objectives and measurement modes, J. Atmos. Sci., 56, 127–150, 1999. 12178

Fell, F. and Fischer, J.: Numerical simulation of the light field in the atmosphere–ocean system using the matrix-operator method, J. Quant. Spectrosc. Ra., 69, 351–388, doi:10.1016/S0022-4073(00)00089-3, 2001. 12188

Frankenberg, C., Butz, A., and Toon, G. C.: Disentangling chlorophyll fluorescence from atmospheric scattering effects in O_2 A-band spectra of reflected sun-light, Geophys. Res. Lett., 38, L03801, doi:10.1029/2010GL045896, 2011a. 12182

Frankenberg, C., Fisher, J. B., Worden, J., Badgley, G., Saatchi, S. S., Lee, J., Toon, G. C., Butz, A., Jung, M., Kuze, A., and Yokota, T.: New global observations of the terrestrial carbon

AMTD
7, 12173–12217, 2014

cycle from GOSAT: Patterns of plant fluorescence with gross primary productivity, Geophys. Res. Lett., 38, L17706, doi:10.1029/2011GL048738, 2011b. 12175

Frankenberg, C., O'Dell, C., Guanter, L., and McDuffie, J.: Remote sensing of near-infrared chlorophyll fluorescence from space in scattering atmospheres: implications for its retrieval and interferences with atmospheric CO_2 retrievals, Atmos. Meas. Tech., 5, 2081–2094, doi:10.5194/amt-5-2081-2012, 2012. 12189, 12192

Friedl, M. A., McIver, D. K., Hodges, J. C. F., Zhang, X., Muchoney, D., Strahler, A. H., Woodcock, C. E., Gopal, S., Schneider, A., Cooper, A., Baccini, A., Gao, F., and Schaaf, C.: Global land cover mapping from MODIS: algorithms and early results, Remote Sens. Environ., 83, 287–302, 2002. 12181, 12195, 12199

Guanter, L., Frankenberg, C., Dudhia, A., Lewis, P., Gómez-Dans, J., Kuze, A., Suto, H., and Grainger, R. G.: Retrieval and global assessment of terrestrial chlorophyll fluorescence from GOSAT space measurements, Remote Sens. Environ., 121, 236–251, doi:10.1016/j.rse.2012.02.006, 2012. 12175, 12176

Guanter, L., Rossini, M., Colombo, R., Meroni, M., Frankenberg, C., Lee, J., and Joiner, J.: Using field spectroscopy to assess the potential of statistical approaches for the retrieval of sun-induced chlorophyll fluorescence from ground and space, Remote Sens. Environ., 133, 52–61, doi:10.1016/j.rse.2013.01.017, 2013. 12176

Guanter, L., Zhang, Y., Jung, M., Joiner, J., Voigt, M., Berry, J. A., Frankenberg, C., Huete, A. R., Zarco-Tejada, P., Lee, J., Moran, M., Ponce-Campos, G., Beer, C., Camps-Valls, G., Buchmann, N., Gianelle, D., Klumpp, K., Cescatti, A., Baker, J., and Griffis, T.: Global and time-resolved monitoring of crop photosynthesis with chlorophyll fluorescence, P. Natl. Acad. Sci. USA, 111, E1327–E1333, 2014a. 12194

Guanter, L., Aben, I., Tol, P., Krijger, M., Hollstein, A., Köhler, P., Damm, A., Frankenberg, C., and Joiner, J.: Potential of the TROPOspheric Monitoring Instrument (TROPOMI) onboard the Sentinel-5 Precursor for the monitoring of terrestrial chlorophyll fluorescence, Atmos. Meas. Tech. Discuss., submitted, 2014b. 12189, 12192

Joiner, J., Yoshida, Y., Vasilkov, A. P., Yoshida, Y., Corp, L. A., and Middleton, E. M.: First observations of global and seasonal terrestrial chlorophyll fluorescence from space, Biogeosciences, 8, 637–651, doi:10.5194/bg-8-637-2011, 2011. 12175

Joiner, J., Yoshida, Y., Vasilkov, A. P., Middleton, E. M., Campbell, P. K. E., Yoshida, Y., Kuze, A., and Corp, L. A.: Filling-in of near-infrared solar lines by terrestrial fluorescence and other geo-

AMTD
7, 12173–12217, 2014

physical effects: simulations and space-based observations from SCIAMACHY and GOSAT, Atmos. Meas. Tech., 5, 809–829, doi:10.5194/amt-5-809-2012, 2012. 12175, 12176

Joiner, J., Guanter, L., Lindstrot, R., Voigt, M., Vasilkov, A. P., Middleton, E. M., Huemmrich, K. F., Yoshida, Y., and Frankenberg, C.: Global monitoring of terrestrial chlorophyll fluorescence from moderate-spectral-resolution near-infrared satellite measurements: methodology, simulations, and application to GOME-2, Atmos. Meas. Tech., 6, 2803–2823, doi:10.5194/amt-6-2803-2013, 2013. 12174, 12176, 12177, 12179, 12180, 12182, 12183, 12184, 12185, 12188, 12191, 12192, 12194, 12195, 12196, 12197, 12200, 12210, 12213, 12214

Lichtenberg, G., Kleipool, Q., Krijger, J. M., van Soest, G., van Hees, R., Tilstra, L. G., Acarreta, J. R., Aben, I., Ahlers, B., Bovensmann, H., Chance, K., Gloudemans, A. M. S., Hoogeveen, R. W. M., Jongma, R. T. N., Noël, S., Piters, A., Schrijver, H., Schrijvers, C., Sioris, C. E., Skupin, J., Slijkhuis, S., Stammes, P., and Wuttke, M.: SCIAMACHY Level 1 data: calibration concept and in-flight calibration, Atmos. Chem. Phys., 6, 5347–5367, doi:10.5194/acp-6-5347-2006, 2006. 12178

Meroni, M., Rossini, M., Guanter, L., Alonso, L., Rascher, U., Colombo, R., and Moreno, J.: Remote sensing of solar-induced chlorophyll fluorescence: review of methods and applications, Remote Sens. Environ., 113, 2037–2051, doi:10.1016/j.rse.2009.05.003, 2009. 12174

Munro, R., Eisinger, M., Anderson, C., Callies, J., Corpaccioli, E., Lang, R., Lefebvre, A., Livschitz, Y., and Pérez Albiñana, A.: GOME-2 on MetOp, in: Atmospheric Science Conference, Vol. 628 of ESA Special Publication, 2006. 12177

Sanders, A. F. J. and de Haan, J. F.: Retrieval of aerosol parameters from the oxygen A band in the presence of chlorophyll fluorescence, Atmos. Meas. Tech., 6, 2725–2740, doi:10.5194/amt-6-2725-2013, 2013. 12186

Schwarz, G.: Estimating the dimension of a model, Ann. Stat., 6, 461–464, doi:10.1214/aos/1176344136, 1978. 12185

Tucker, C. J.: Red and photographic infrared linear combinations for monitoring vegetation, Remote Sens. Environ., 8, 127–150, doi:10.1016/0034-4257(79)90013-0, 1979. 12192

Wang, P., Stammes, P., van der A, R., Pinardi, G., and van Roozendael, M.: FRESCO+: an improved O_2 A-band cloud retrieval algorithm for tropospheric trace gas retrievals, Atmos. Chem. Phys., 8, 6565–6576, doi:10.5194/acp-8-6565-2008, 2008. 12181

AMTD
7, 12173–12217, 2014

Zarco-Tejada, P., Pushnik, J., Dobrowski, S., and Ustin, S.: Steady-state chlorophyll a fluorescence detection from canopy derivative reflectance and double-peak red-edge effects, Remote Sens. Environ., 84, 283–294, doi:10.1016/S0034-4257(02)00113-X, 2003. 12174

AMTD
7, 12173–12217, 2014

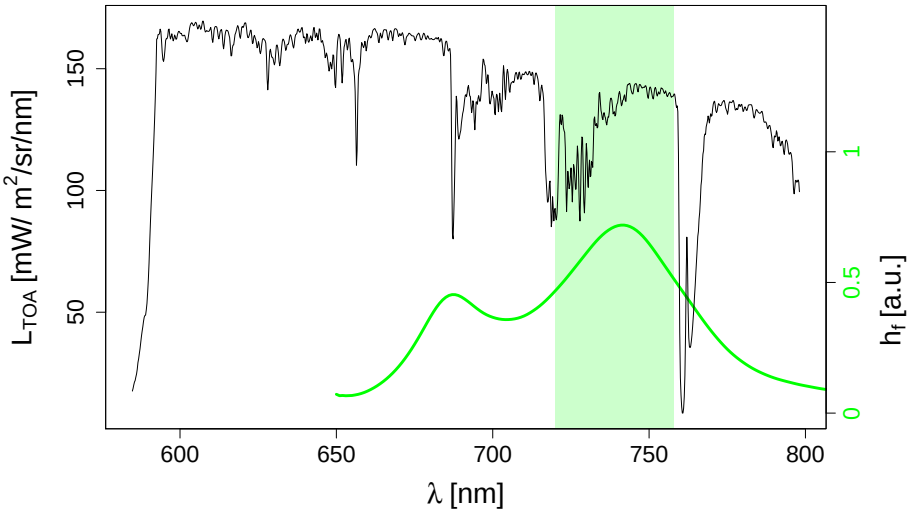

Figure 1. Sample GOME-2 spectrum in band 4. The spectral window that we use for SIF retrievals (720–758 nm) is marked in green. The reference fluorescence emission spectrum is depicted in green as well.

AMTD
7, 12173–12217, 2014

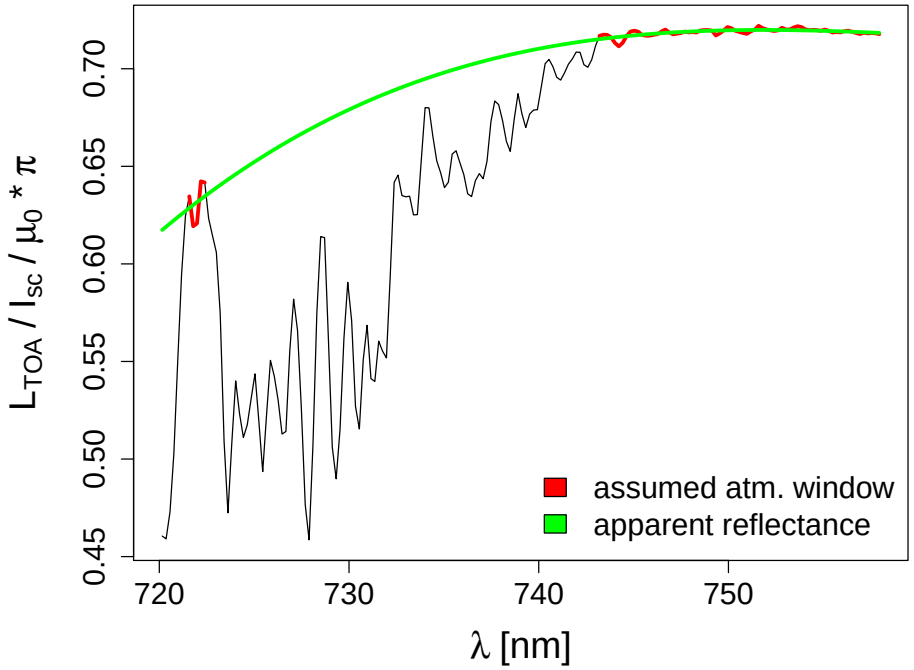

Figure 2. Estimation of apparent reflectance (green) from a sample GOME-2 measurement in the 720–758 nm fitting window by a third order polynomial using atmospheric windows (red).

AMTD
7, 12173–12217, 2014

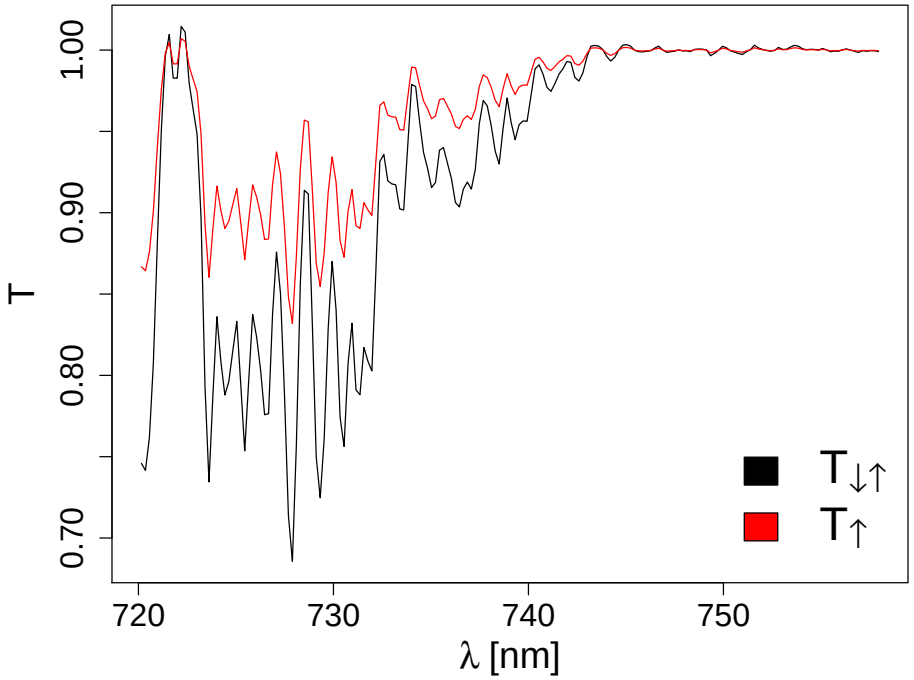

Figure 3. Estimation of the total atmospheric transmission in down- and upward direction (black) and in upward direction (red) using Eq. (4) from a sample GOME-2 measurement in the 720–758 nm fitting window.

AMTD
7, 12173–12217, 2014

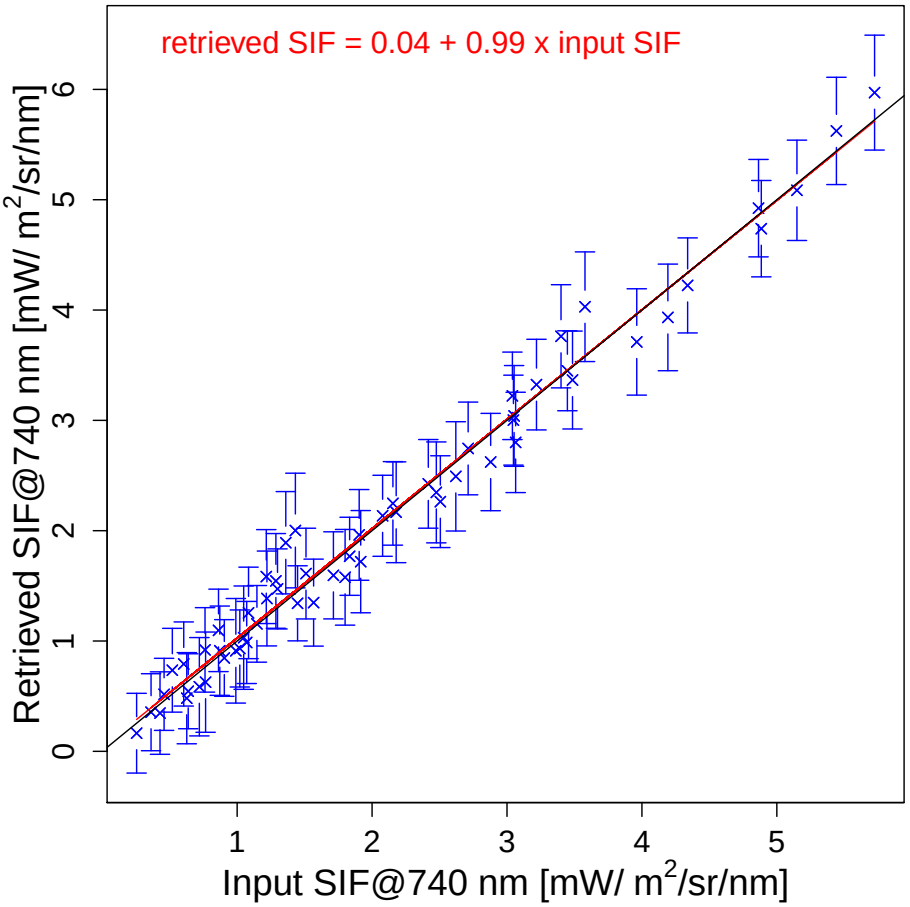

Figure 4. Input vs. retrieved SIF at 740 nm of the end-to-end simulation using the retrieval window from 720–758 nm and 8 PCs. The average of the retrieved SIF for each top-of-canopy (TOC) is shown together with its SD (errorbar). A linear fit of all TOC means is shown in red.

AMTD
7, 12173–12217, 2014

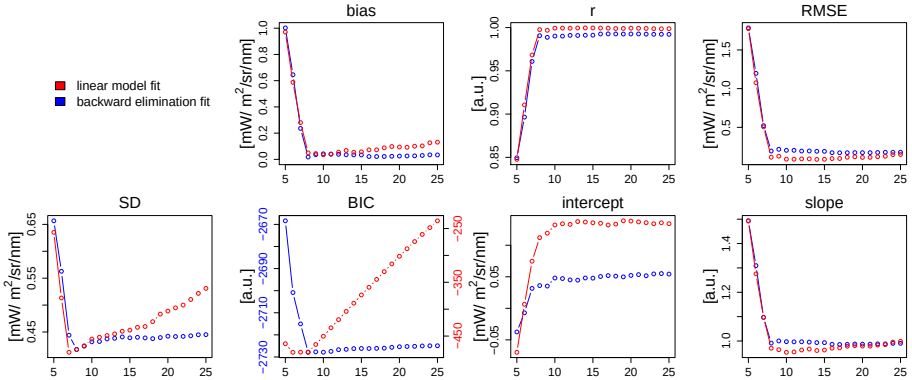

Figure 5. Various statistical comparisons of retrieved values of SIF at 740 nm obtained with simulated data for the linear model fit using all potential coefficients (red) and the backward elimination fit (blue) in dependence of the provided number of PCs (x axis). Depicted are bias (mean difference of retrieved minus input SIF), correlation between retrieved and input SIF (r), the root-mean-square error of the SIF retrievals (RMSE), the SD of retrieved SIF values (SD), the mean Bayesian information criterion (BIC), intercept and slope of a linear fit (retrieved SIF = intercept + slope · input SIF)

AMTD
7, 12173–12217, 2014

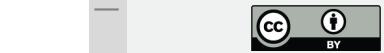

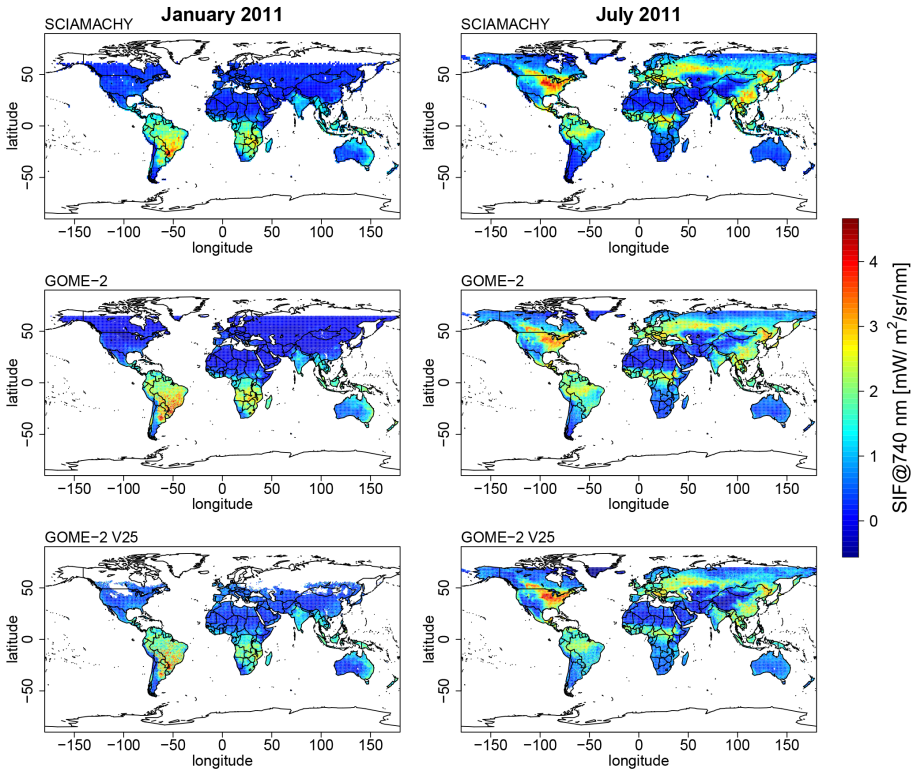

Figure 6. Monthly composites of SIF at 740 nm for January (left column) and July (right column) 2011. The upper line depicts SIF results using SCIAMACHY data and the lines below show SIF composites derived from GOME-2 data using our algorithm (middle line) and SIF results provided by Joiner et al. (2013) (bottom line). The SCIAMACHY composites and results from Joiner et al. (2013) are scaled by the relationships found in Figs. 7 and 9 respectively, in order to ensure a visual comparability.

AMTD
7, 12173–12217, 2014

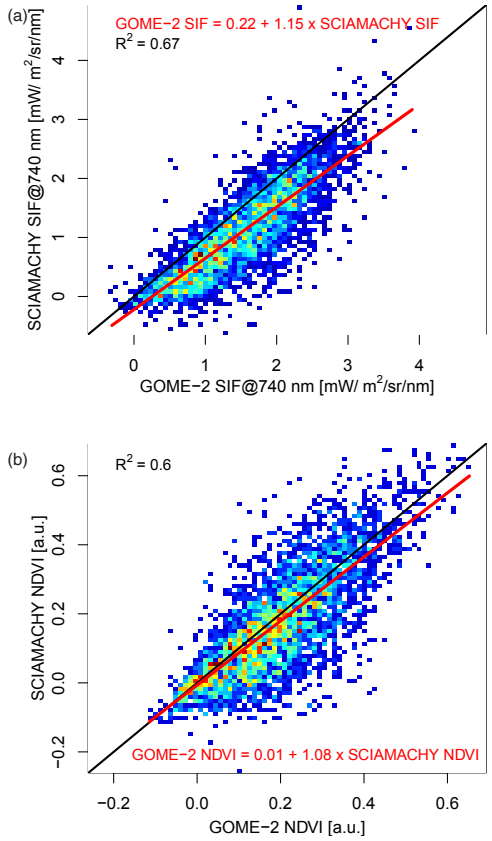

Figure 7. Scatter plots of **(a)** SIF and **(b)** NDVI obtained from GOME-2 and SCIAMACHY data for July 2011. Evaluated are only measurements which are classified as vegetated (IGBP land classification) with a cloud fraction lower than 0.5. A linear fit is depicted in red. The color changes from blue to red, the more points occur for one value.

AMTD
7, 12173–12217, 2014

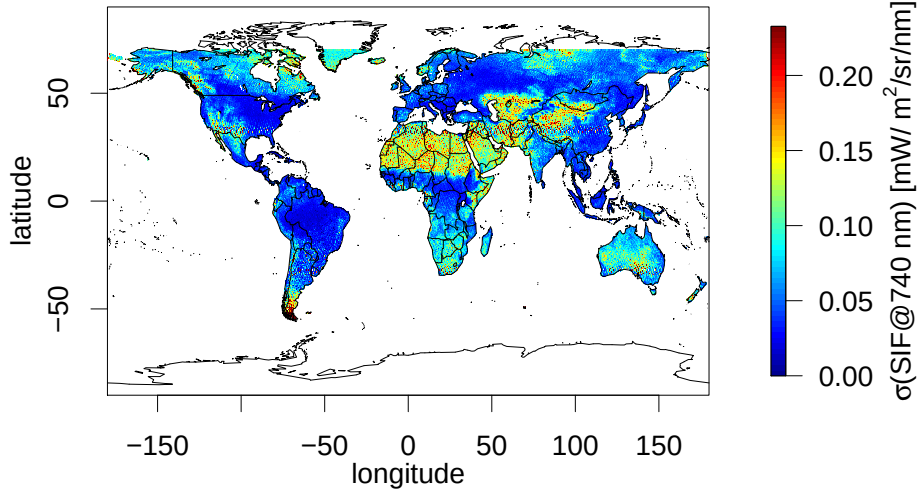

Figure 8. Standard error (using Eq. 11) of the monthly composite of GOME-2 SIF for July 2011.

AMTD
7, 12173–12217, 2014

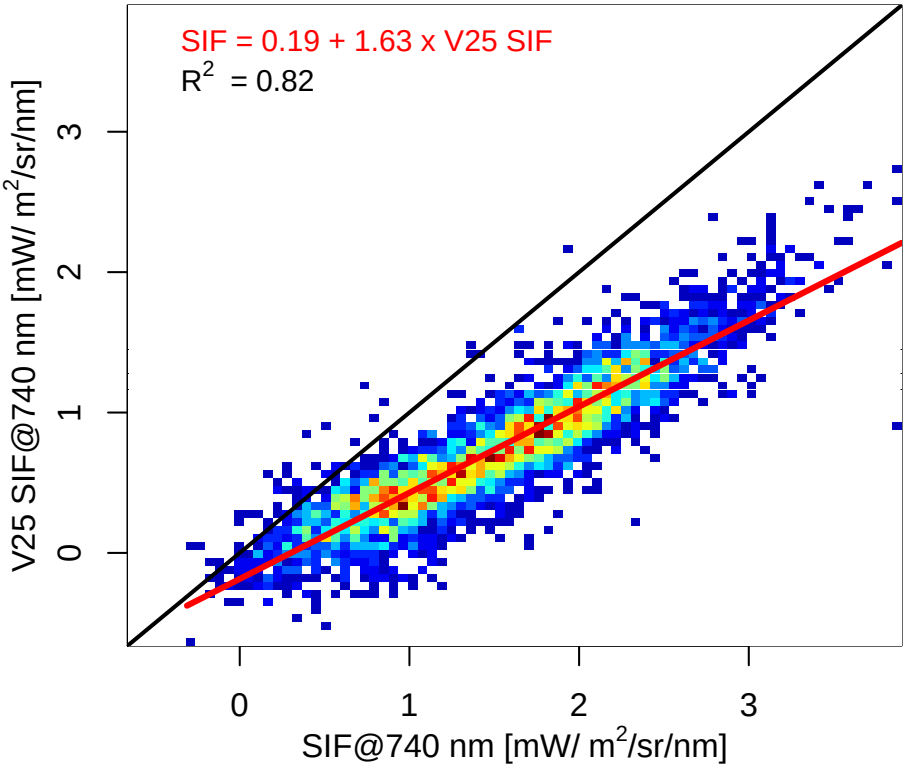

Figure 9. Scatter plot of SIF derived with the presented algorithm and the V25 algorithm from Joiner et al. (2013) for July 2011. Similar to Fig. 7 only measurements which are classified as vegetated (IGBP land classification) with a cloud fraction lower than 0.5 are evaluated. A linear fit is depicted in red. The color changes from blue to red, the more points occur for one value.

AMTD
7, 12173–12217, 2014

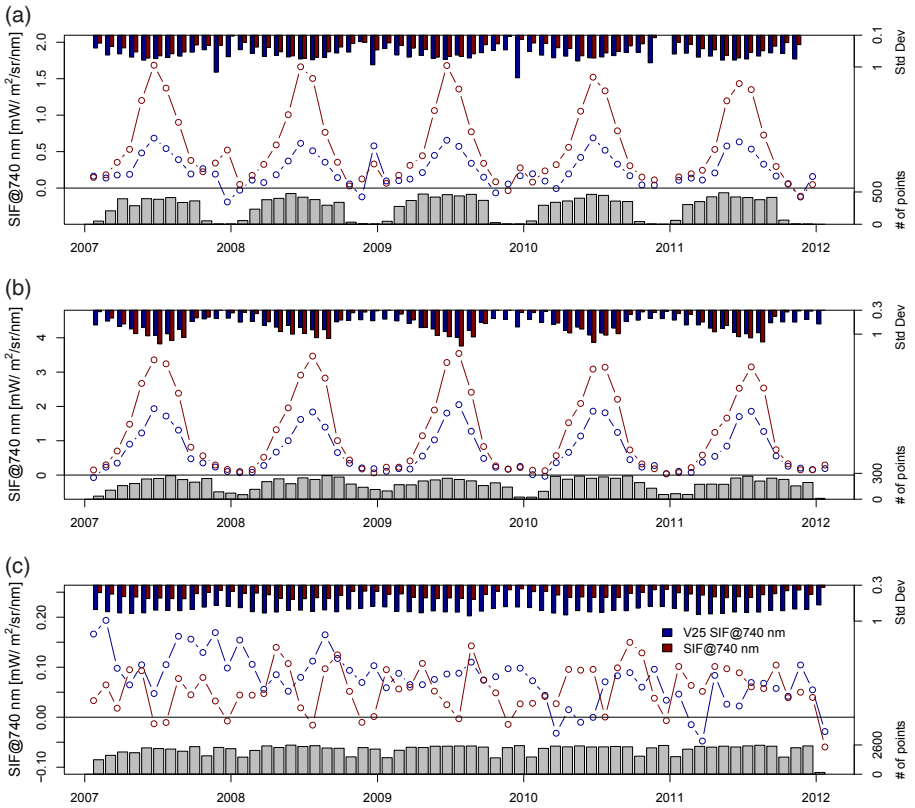

Figure 10. Comparison between monthly means of SIF derived from GOME-2 data using collocated retrieval results from Joiner et al. (2013) (V25; blue) and the presented algorithm (red). Time series for three different IGBP land classification types in dedicated areas are shown. The SD or fluctuation (top) and the number of included retrievals (bottom) per time step are depicted as barplots in each subfigure. **(a)** Evergreen needleleaf forest between 0–180° E, 45–75° N. **(b)** Croplands between 100–80° W, 35–50° N. **(c)** Barren or sparsely vegetated areas between 20° W–35° E, 15–35° N.

AMTD
7, 12173–12217, 2014

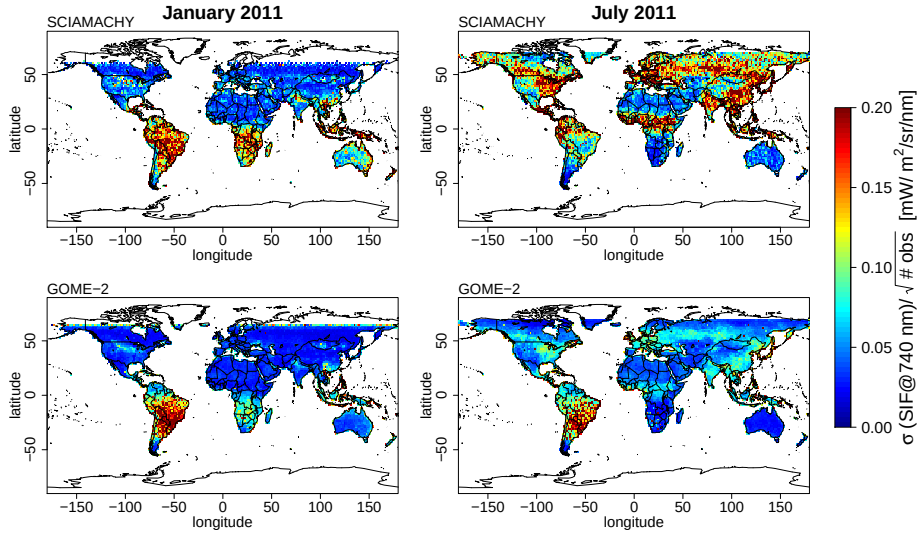

Figure 11. Monthly composites of the SD (SD) using Eq. (9) of SIF for January (left column) and July (right column) 2011 derived from SCIAMACHY (top) and GOME-2 data (bottom) in a spatial resolution of 1.5° × 1.5°. The underlying SCIAMACHY SIF values are again scaled by the relationship found in Fig. 7 in order to ensure a comparability.

AMTD
7, 12173–12217, 2014

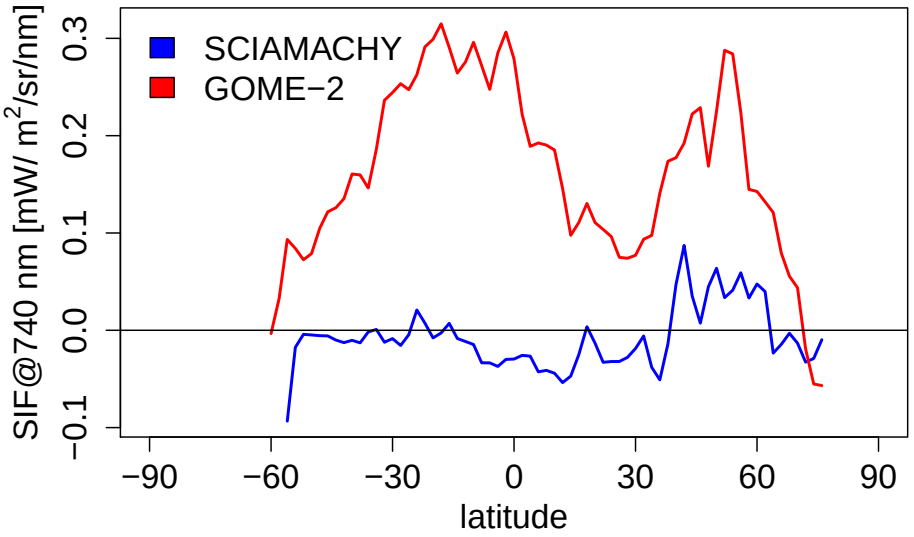

Figure 12. Mean SIF of training set derived with data from GOME-2 and SCIAMACHY averaged over latitudes for July 2011.

AMTD
7, 12173–12217, 2014

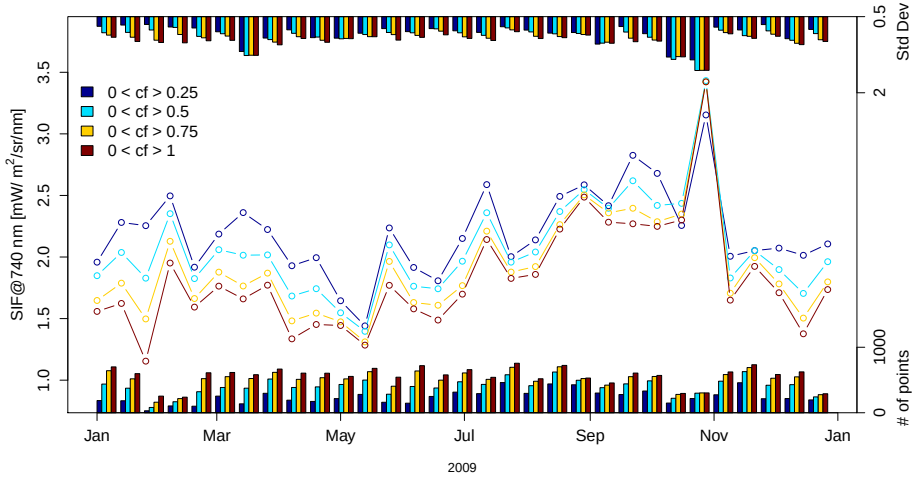

Figure 13. Temporal series of SIF retrievals from GOME-2 data over a box in the Amazon Basin (70–65° W, 5–0° S, covered with evergreen broadleaf forest) for different cloud fraction thresholds. The time series corresponds to 12 day means in 2009. The SD (top) and the number of included retrievals (bottom) per time step are depicted as barplots.

AMTD
7, 12173–12217, 2014